ISME - Incoherent Sampling of Multi-Echo data to minimize cardiac-induced noise in brain maps of R_2* and magnetic susceptibility

Quentin Raynaud[1*], Rita Oliveira[1*], Nadège Corbin[2], Yaël Balbastre[3], Ruud B. van Heeswijk[4], Antoine Lutti[1]

[1]*Laboratory for Research in Neuroimaging, Department for Clinical Neuroscience, Lausanne University Hospital and University of Lausanne, Lausanne, Switzerland*

[2]*Centre de Résonance Magnétique des Systèmes Biologiques, UMR5536, CNRS/University Bordeaux, Bordeaux, France*

[3]*Department of Experimental Psychology, University College London, London, United Kingdom*

[4]*Department of Diagnostic and Interventional Radiology, Lausanne University Hospital and University of Lausanne, Lausanne, Switzerland.*

*These authors contributed equally to this work.

Correspondence

Antoine Lutti

Laboratory for Research in Neuroimaging, Department for Clinical Neuroscience, Lausanne University Hospital, Ch. de Mont-Paisible 16, CH-1011 Lausanne

Email: antoine.lutti@chuv.ch

Abstract

Purpose

Maps of the MRI parameters R_2* and magnetic susceptibility (χ) enable the investigation of microscopic tissue changes in brain disease. However, cardiac-induced signal instabilities increase the variability of brain maps of R_2* and χ. In this study, we introduce ISME – a sampling strategy that minimizes the level of cardiac-induced instabilities in brain maps of R_2* and χ.

Methods

ISME uses phase-encoding gradients to shift the k-space frequency of the acquired data between consecutive readouts of a multi-echo train. As a result, the multi-echo data at a given k-space index is acquired at different phases of the cardiac cycle. We compare the variability of R_2* and χ maps acquired with ISME and with standard multi-echo trajectories in N=10 healthy volunteers. We investigate the effect of both trajectories on the spatial aliasing of pulsating MR signals and propose a weighted-least squares (NWLS) approach for the estimation of R_2* that accounts for the increase of the residuals with echo time.

Results

ISME reduces the variability of R_2* and χ maps across repetitions by 25/26/21% and 24/32/23% in the cerebellum/brainstem/whole brain, respectively. With ISME, the spatial aliasing of pulsating MR signals is incoherent between raw echo images, leading to visually sharper R_2* maps. The proposed NWLS approach for the estimation of R_2* reduces the dependence of the fitting residuals on echo time and the variability of R_2* by an additional 3/2/1% in the cerebellum/brainstem/whole brain.

Conclusion

ISME allows the mitigation of cardiac-induced signal instabilities in brain maps of R_2* and χ, improving reproducibility.

Keywords:

Brain; cardiac-induced noise; Physiological noise; quantitative MRI; R2*; QSM; MRI relaxometry;

1. Introduction

The transverse relaxation rate ($R_2^* = 1/T_2^*$)[1] and magnetic susceptibility (χ)[2] are markers of iron and myelin content within brain tissue[3,4] and allow the study of microscopic tissue change due to brain disease in patient populations.[5–7] Maximal reproducibility is required of R_2^* and χ maps to allow optimal sensitivity to brain change in neuroscience studies. In addition to thermal noise,[8,9] MRI data reproducibility is affected by signal instabilities of physiological origin.[10,11] Respiration and cardiac pulsation are the primary sources of physiological signal instabilities, which can also cause image aliasing or blurring.[12,13] Physiological signal instabilities increase with the echo time used for data acquisition.[14,15] Gradient-recalled echo (GRE) data used for R_2^* and χ mapping typically reach echo times of up to ~40ms[7,16,17] and are therefore particularly sensitive to physiological signal instabilities.[16,18]

Respiration-induced signal instabilities originates from periodic fluctuations of the magnetic field due to changes in air volume in the lungs.[19] The effects of respiration on brain MRI data are typically corrected using phase navigators that reduce the variability of R_2^* and χ maps by 23% and 12% across repetitions in white matter.[16] Cardiac-induced signal instabilities are the result of multiple physiological mechanisms: cardiac pulsation generates a pressure wave that leads to head motion,[20] CSF pulsation[21,22] and deformation[23,24] of inferior regions such as the brainstem[25,26] and cerebellum.[27] Also, pulsatile vessel movement and periodic blood influx[28–32] lead to spatially-localized effects that are most pronounced in highly vascularized regions such as the orbitofrontal cortex[22,33] and periventricular regions.[33,34] Physiological effects that are coherent across a voxel, such as variation of the mean magnetic field across a voxel,[16,35] laminar flow,[36,37] and motion[38–40] result in a net phase shift of the signal and primarily affect magnetic susceptibility estimates. On the other hand, effects that are incoherent across a voxel (e.g. turbulent flow,[41] local B_0 inhomogeneities[42]) result in a net change of the magnitude of the signal and primarily affect R_2^* estimates. Cardiac pulsation has recently been reported to lead to variations of R_2^* by up to $3s^{-1}$ across the cardiac cycle and to account for ~35% of the variability of R_2^* maps across repetitions.[18]

The acquisition of R_2^* and χ data stretches over several minutes. Cardiac-induced signal instabilities cannot be regressed out retrospectively from the temporal evolution of the signal as is routinely done for functional MRI data.[12,43,44] Also, the effects of cardiac pulsation on the MR signal are spatially localized and are not compatible with the navigator techniques used for the correction of respiration- or motion-induced effects.[45,46] Instead, prospective strategies show promising potential to reduce the impact of cardiac-induced signal instabilities in the acquired data. Specially-designed k-space sampling trajectories lead to spatially-incoherent aliasing of cardiac-induced signal instabilities across the field of view of an individual image.[47,48] Setting the number of samples at each k-space index according to the local amplitude of the signal instabilities is effective to improve the reproducibility of R_2^*-mapping data.[49] However it does not consider the effect of cardiac-induced signal instabilities across the temporal dimension of the multi-echo data.

In this study, we introduce a new sampling strategy to reduce the level of cardiac-induced signal instabilities in multi-echo data used for the computation of R_2^* and χ maps. This sampling strategy is based on dispersing the effect of the instabilities along the temporal dimension of the multi-echo data: with ISME (Incoherent Sampling of Multi-Echo data), the k-space frequency of the acquired data is changed between consecutive readouts of the echo train. As a result, the multi-echo data at a given k-space index are acquired across different phases of the cardiac cycle. The goal of this study was to demonstrate that ISME leads to higher reproducibility of brain maps of R_2^* and χ than standard k-space sampling trajectories in healthy volunteers. We also investigated the effect of both sampling

strategies on the spatial aliasing of cardiac pulsation effects in maps of R_2* and χ and on the fitting residuals.

2. Methods

2.1. ISME

With standard multi-echo trajectories, data are acquired at a single k-space frequency after each radiofrequency (RF) excitation. To allow for full image encoding, this process is repeated across a suitable set of k-space frequencies. Because the repetition time is much smaller than the cardiac period (TR $\lesssim$ 50ms), the multi-echo data at each k-space frequency can be assumed to have been acquired at the same phase of the cardiac cycle (Figure 1A). Because cardiac pulsation leads to systematic changes of R_2* across the cardiac cycle,[18] this multi-echo data contains exponential-like effects of cardiac pulsation on signal decay, leading to a bias of the apparent R_2*. This bias depends on the phase of the cardiac cycle at the time of acquisition of the data (Figure 1B). To minimize the effect of cardiac pulsation on R_2* estimates, we introduce ISME (Incoherent Sampling of Multi-Echo data) - a new sampling strategy that allows to sample the cardiac phase incoherently along the echo dimension. With ISME, short gradient pulses are played out between each readout of the multi-echo train to shift the k-space index (Figure 1C). Upon completion of data acquisition, the data at each k-space index is made up of multiple echoes acquired at different phases of the cardiac cycle. With ISME, estimation of R_2* averages out the fluctuations of signal decay across the cardiac cycle, at the cost of larger fit residuals (Figure 1D).

In this conceptual description of ISME, the k-space index is a simple counter that reflects the sequential ordering of data sampling. It is independent of the physical coordinates of the k-space frequencies and of the k-space trajectory used for data acquisition (e.g. linear, spiral or radial). Also, the time span between consecutive indexes might be a single TR interval in the case of two data points acquired consecutively, or a longer time interval. Here, we consider the case of a 3D FLASH sequence with linear sampling, in which neighbouring points are acquired consecutively along the fast phase-encoding direction, for each phase-encoding step along the slow direction. With this trajectory, the time interval between consecutive data points along the fast phase-encoding direction is TR $\lesssim$ 50ms, much shorter than the typical cardiac period. Cardiac pulsation leads to a broad modulation of the MR signal across k-space along this phase-encoding direction. We therefore implemented ISME along the slow phase-encoding direction, for which the time interval between neighbouring points is $TR*N_{fast}$, where N_{fast} is the number of k-space indexes along the fast encoding direction. The pulse diagram of the ISME GRE sequence is illustrated in figure 1E. With ISME, the shift of the k-space index is implemented by means of short gradient pulses ('*blips*') along the slow phase-encode direction, as in Echo Planar Imaging (EPI).[50] However, unlike EPI, the data from the consecutive readouts of the multi-echo train are stored separately to obtain an individual image at each echo time. To reduce acquisition time, appropriate modulation of the amplitude of the blip gradients allows undersampling of k-space according to e.g. the GRAPPA[51] or CAIPIRINHA[52] filling patterns used for Echo Planar Time-resolved Imaging (EPTI)[53,54] or segmented EPI.[55,56]

With ISME, the multi-echo data at a single k-space index is acquired over a duration $TR*N_{fast}*N_{echo}$, where N_{echo} is the number of echoes. To fully populate the k-TE space of the data with the diagonal sampling pattern of ISME (top-left and bottom right corners of Figure 1C), the sampling trajectory of ISME is initiated beyond the k-space boundary determined from the image encoding parameters, at $k=-(N_{echo}-1)$ and $k=k_{end}-(N_{echo}-1)$. The RF receivers are blanked in this region of k-space (shaded areas of Figure 1C), resulting in an increase of scan time by $TR*N_{fast}*(N_{echo}-1)$.

2.2. MRI data acquisition

Eleven healthy volunteers (4 females, mean age=33±9 years old) were scanned on a 3T MRI system (Magnetom Prisma; Siemens Medical Systems, Erlangen, Germany) using a 64-channel head coil. Written informed consent was obtained from each participant prior to participation and the study was approved by the local ethics committee. The data from one participant was excluded from analysis due to strong motion artifacts (Supplementary material 1). Acquisition of the GRE data was conducted using a custom-made multi-echo 3D FLASH pulse sequence. The k-space trajectory was linear Cartesian. The main acquisition parameters are highlighted in Table 1. 14 echo images were acquired with a bipolar readout, with echo times TE=1.25ms to 16.85ms with 1.2ms echo spacing (protocol 1). The repetition time was TR=21ms, the RF excitation angle 12°, the voxel size was 1.2x1.2x1.2mm^3 and the field of view 208×192×144mm^3. The images were reconstructed on the MRI scanner with adaptive coil combination[57,58] and GRAPPA[51] with an acceleration factor of 2. Phase navigators were used to correct for systematic phase differences between positive and negative readouts.[59] In pilot experiments, ISME was observed to mitigate aliasing artefacts of non-cardiac origin such as those due to eye movement (Supplementary material 2). To keep the focus of this study specifically on cardiac-induced effects, the imaging volume was tilted by 30 degrees in the sagittal plane to displace this artefact below the brain. The total scan time was 5:29 minutes for the standard multi-echo trajectory and 6:08 minutes (+12%) for ISME due to the k-space boundary excursions. In experiment 1, each sampling strategy was acquired 3 times, in a randomized order, to quantify the reproducibility of the data across repetitions. In experiment 2, one of the participants (male, 31 years old) underwent an additional MRI exam with protocol 1. To assess the incoherent averaging of cardiac-induced signal instabilities across multiple repetitions of the standard multi-echo trajectory, experiment 2 involved 9 repetitions of data acquisition with the standard multi-echo trajectory and 3 repetitions of data acquisition with ISME.

One of the participants (male, 44 years old) underwent an additional MRI exam at a higher resolution of 0.8x0.8x0.8mm^3 (protocol 2, see Table 1; other parameters the same as above). No tilt of the imaging volume was used). During this exam, one multi-echo dataset with the standard multi-echo trajectory (18:52 minutes) and one with the proposed ISME (20:28 minutes, +8%) were acquired. This data is available online (10.5281/zenodo.13364051).

To allow accurate tissue segmentation and delineation of grey matter regions, a multi-parameter relaxometry protocol was also used for the acquisition of multi-echo 3D FLASH data with magnetization transfer (MT), proton density (PD) and T1-weighted contrast (RF excitation angle = 6°, 6° and 21° respectively; TR/TE=24.5/2.34ms; voxel size: 1.5x1.5x1.5mm^3; field of view: 176×240×256mm^3). 8 echo images were acquired for the T1- and PD-weighted contrasts and 6 for the MT-weighted contrast. B_1-field mapping data (voxel size: 4x4x4mm^3; TR/TE=200/39.1ms) and B_0-field mapping data (voxel size: 3x3x2.5mm^3; TR=700ms; TE_1/TE_2=4.92/7.38ms) were also acquired.[60,61]

2.3. Image segmentation

Maps of MTsat[62] were computed from the MT-, PD- and T1-weighted images using the hMRI toolbox (https://hMRI.info).[63] The MTsat maps and GRE data acquired with the standard multi-echo trajectory and ISME were co-registered using Statistical Parametric Mapping (SPM12, Wellcome Centre for Human Neuroimaging, London, UK).

Grey and white matter probabilities maps were obtained from the segmentation of the MTsat maps with SPM Unified Segmentation.[64–66] Whole-brain masks were defined from the voxels with a grey or white matter probability above 0.95. Because B_0-field inhomogeneities affect the transverse decay of the MR signal,[67] voxels in the proximity of the air/tissue interface (e.g. orbitofrontal cortex, amygdala, temporal lobe, hippocampus) were removed from the masks. Brainstem and cerebellum regions of

interest (ROIs), in close proximity to the ventricles, carotid arteries and large blood vessels were defined from the labelled data provided by Neuromorphometrics, Inc. (http://neuromorphometrics.com/) under academic subscription, and were set to contain voxels with a grey or white matter probability above 0.95. Additional occipital, frontal, parietal and temporal grey matter ROIs were also computed from the Neuromorphometrics atlas. White matter ROIs of the corticospinal tract, inferior longitudinal fasciculus and optic radiation were computed from the JHU DTI-based atlases (https://identifiers.org/neurovault.collection:264).[68–70]

2.4. Relaxometry

Data were analysed using bespoke analysis scripts written in MATLAB R2021a (The Mathworks, Natick, MA). Before the estimation of R_2*, the distribution of signal intensities in the background voxels of the magnitude images was fitted with a Rician distribution. The value of the noncentrality parameter was deducted from the signal intensities to suppress the noise floor in these images.[71–73] The signal intensities in each voxel of the magnitude images were then fitted with the following model:

$$S(TE) = S_0 \exp(-R_2^* TE) + \varepsilon \quad [1]$$

where S_0 is the signal amplitude at $TE = 0$ and ε is the residual error. Fitting was conducted using the non-linear least square (NLS) *lsqnonlin* MATLAB function with a trust-region-reflective algorithm. R_2* was bounded between 1 to 80s^{-1} and its initial value was 20s^{-1}. The root-mean-squared error (RMSE) of the fit was computed as a measure of the lack of fit. To investigate the effect of the number of echoes, R_2* estimation was conducted using all 14 acquired echo data, 7 echoes (echo numbers 1, 3, 5, 7, 9, 11 and 13), 5 echoes (echo numbers 1, 4, 7, 10 and 13), 4 echoes (echo numbers 1, 5, 9, 13) and 3 echoes (echo numbers 1, 6 and 11).

The NLS approach for the estimation of R_2* assigns an equal contribution of all echo images to the error estimates, regardless of their respective echo times. Alternatively, we also computed maps of R_2* using a nonlinear weighted least squares (NWLS) approach, with weights that reflect the noise level in each individual echo image. Estimation of the image-specific weights was conducted on the model of the QUIQI technique, which addresses the effect of motion degradation on the noise level in image analyses.[74–76] The noise level in the multi-echo data was modelled as a polynomial function of the echo time. The polynomial coefficients were estimated using the implementation of Restricted Maximum Likelihood (ReML) in SPM[77] (Supplementary material 3, Matlab code available online (10.5281/zenodo.14808609)). The optimal order of this polynomial, which maximized the estimates of the evidence lower bound (ELBO) provided by ReML, was 4. The image-specific weights were computed as the inverse of the noise covariance matrix estimated by ReML with the optimal noise model. These weights were then used to estimate R_2* according to eq. [1], using the non-linear least square *lsqnonlin* MATLAB function.

2.5. Quantitative susceptibility mapping

Quantitative magnetic susceptibility maps were generated from the phase of the MR data using bespoke scripts adapted from https://github.com/fil-physics/MPM_QSM. We used ROMEO[78] for the unwrapping of the phase images and ASPIRE[59] to remove the systematic phase differences between odd and even echo images. After segmentation of the first echo magnitude image with SPM's Unified Segmentation,[66] brain masks were defined to include voxels with a combined grey matter, white matter and CSF probability above 0 and with values of the ROMEO[78] phase quality metric above 0.3. Any holes present within the resulting mask were subsequently filled using the MATLAB function *imfill*. The spurious contribution of the background field to the phase data was removed using the Projection onto Dipole Fields algorithm[79] available in the SEPIA toolbox.[80] Finally, dipole inversion was conducted using the STAR-QSM algorithm[81] available in the SEPIA toolbox, using the entire brain as a reference.

To investigate the effect of the number of echoes, QSM estimation was conducted using all 14 acquired echo data, 7 echoes (echo numbers 1, 3, 5, 7, 9, 11 and 13), 5 echoes (echo numbers 1, 4, 7, 10 and 13), 4 echoes (echo numbers 1, 5, 9, 13) and 3 echoes (echo numbers 1, 6 and 11).

2.6. Statistical analyses

The effects of cardiac pulsation on the MR signal lead to changes of the apparent R_2* across the cardiac cycle.[18] With standard multi-echo trajectories, the multi-echo data at a given k-space frequency is acquired for a given phase of the cardiac cycle and cardiac-induced signal instabilities increases the variability of the data across repetitions.[18] With ISME, multi-echo data representative of the whole cardiac cycle are acquired for each repetition (Figure 1). We conducted statistical analyses to test if this leads to reduced data variability compared to standard multi-echo trajectories. Regional estimates of the standard deviation (SD) of R_2* and χ across repetitions were computed as the average in each ROI of the voxel-wise SD values. We conducted paired Student's t-tests of the regional SD estimates, for data acquired using the standard multi-echo trajectory and ISME.

With ISME, the effect of cardiac pulsation on signal decay does not follow the exponential dependence on echo time of data acquired with standard multi-echo trajectories. We conducted statistical analyses to verify that this leads to higher levels of RMSE. Regional estimates of the RMSE were computed as the average in each ROI of the voxel-wise RMSE values obtained from the estimation of R_2*. We conducted paired Student's t-test analyses of the regional RMSE levels, for data acquired using the standard multi-echo trajectory and ISME.

3. Results

In individual echo images acquired using both the standard multi-echo trajectory and ISME, the k-space data along the slow phase encoding direction are acquired at different phases of the cardiac cycle, leading to spatial aliasing of pulsating veins (figure 2A and 2C, data acquired with protocol 2). With the standard multi-echo trajectory, the distribution of the cardiac phase along the slow phase encoding direction is unchanged across echo images (Figure 1A) and the resulting R_2* maps also display spatial aliasing (Figure 2B). With ISME, the distribution of the phase of the cardiac phase along the slow phase encoding direction differs between echo images (Figure 1C) and the R_2* maps computed from the signal decay across echoes show a reduced level of aliasing (Figure 2D).

The SD of R_2* across repetitions can reach up to $5s^{-1}$ in inferior brain regions in data acquired with the standard multi-echo trajectory (Figure 3A). The most affected areas include the cerebellum and brainstems – two of the regions most affected by cardiac-induced signal instabilities.[18] The SD of R_2* is much reduced in inferior brain regions with the ISME approach, leading to variability maps that are more spatially uniform. With ISME, the SD of R_2* across repetitions is reduced by 25, 26, and 21% in the cerebellum, brainstem and whole brain compared to the standard multi-echo trajectory (Figure 3B, $p \leq 0.001$). Regional estimates of the standard deviation of R_2* across repetitions are provided in Table 2. The SD of R_2* across repetitions decreases with an increasing number of echo images used in the estimation of R_2* (N_{echoes}) (Figure 3C). The sharpest decrease takes place for $N_{echoes} \lesssim 7$ and is about twice as large with ISME than with the standard multi-echo trajectory. With the standard multi-echo trajectory, the SD of R_2* maps computed from N_{av}=2 repetitions is comparable to that of ISME with N_{av}=1 repetition, i.e. a 100% scan time increase (Figure 3D).

Much of these observations are also applicable to maps of χ (Figure 4A,B). ISME reduces the SD of χ estimates across repetitions by 24, 32, and 23% in the cerebellum, brainstem, and whole brain, respectively, compared to the standard multi-echo trajectory (Figure 4C, $p \leq 0.001$). Regional estimates of the standard deviation of χ across repetitions are provided in Table 2. The SD of χ across repetitions decreases with an increasing number of echo images used in the estimation of χ. This decrease is

comparable with ISME and with the standard multi-echo trajectory (Figure 4D). The SD across repetitions of χ maps computed from N_{av}=2 and N_{av}=3 datasets acquired with the standard multi-echo trajectory decreases by ~30% and ~36% respectively (Figure 4E).

With the standard multi-echo trajectory, the maps of the RMSE between the multi-echo data and the exponential fits show a sharp decrease from the brain periphery to central brain regions that mirrors the sensitivity profile of the receive coil (Figure 5A). Data acquired with the proposed ISME approach exhibit higher RMSE levels and a high level of spatial aliasing along the slow phase encoding direction. This increase is stronger in inferior brain areas and around the circle of Willis: the RMSE increases by 18, 13 and 15% in the cerebellum, brainstem and whole brain with the ISME approach (Table 2 and Figure 5B, $p \leq 0.001$).

The variance across repetitions of the residual error increases with echo time for both acquisition strategies (Figure 5C). However, this increase is more pronounced with ISME: assuming a linear increase, the slope reaches 0.49, 0.38 and 0.22 [a.u./ms] in the cerebellum, brainstem and whole brain with ISME and 0.23, 0.17 and 0.06 [a.u./ms] with the standard multi-echo trajectory in these regions (Figure 5D).

The proposed NWLS approach computes weights that are lower at long echo times due to the higher noise level in the corresponding echo images (Figure 6A). Using the NWLS approach to estimate R_2* improves the distribution of the residuals across echo times in data acquired with ISME. However a coherent pattern, with higher residuals at intermediate echo times, remain (Figure 6B). Assuming a linear increase of the residual level with echo time, the slope reduces to 0.05, 0.03 and 0.19 [a.u./ms] in the cerebellum, brainstem and whole brain (0.49, 0.38 and 0.22 [a.u./ms] with NLS, see above) (Figure 6C). The proposed NWLS approach further reduces the SD of R_2* by 3% in the cerebellum, 2% in the brainstem and 1% in the whole-brain compared to the standard NLS (Table 2, $p \leq 0.001$).

4. Discussion

Cardiac pulsation generates exponential-like effects on the transverse decay of multi-echo GRE data, leading to systematic changes of R_2* across the cardiac cycle[18]. With standard trajectories, the multi-echo data is acquired at the same phase of the cardiac cycle, for each k-space frequency, leading to a bias on the R_2* estimates. Because the effect of cardiac pulsation depends on the timing of data acquisition relative to the cardiac cycle, cardiac-induced signal instabilities increase the variability of brain maps of the transverse relaxation rate (R_2*) and quantitative susceptibility (QSM) across repetitions. In this work, we proposed a new sampling strategy termed Incoherent Sampling of Multi-Echo data (ISME), based on shifting k-space location between each readout of the multi-echo train. With ISME, the multi-echo data of each k-space frequency is made up of points acquired at different phases of the cardiac cycle, mitigating the effects of cardiac pulsation across echoes.

With ISME, estimation of R_2* and χ effectively averages out the effect of cardiac pulsation and leads to improved repeatability of the data across repetitions: over the whole brain, ISME reduces the variability of R_2* across repetitions by 21% compared to standard multi-echo trajectories. Similarly, the variability of χ estimates is reduced by 23% with ISME. The reduction in variability were most pronounced in inferior brain regions such as the brainstem and cerebellum (25-26% for R_2* maps and 24-32% for χ maps). With standard multi-echo trajectories, a comparable reduction in variability requires the computation of R_2* maps across 2 averages and a 100% increase in scan time. The SD of R_2* and χ across repetitions decreases when the number of echo images used in their estimation increases. With ISME, the sharper decrease of the variability of R_2* is consistent with the improved

sampling of cardiac-induced signal instabilities across echo images. Around 7 echo images are required in the multi-echo data to achieve near-optimal reduction of the variability of R_2* across repetitions. Maps of the SD of R_2* and χ estimates across repetitions are spatially more uniform with ISME. This reduction of the variability of R_2* and χ maps is similar to that from an alternative sampling strategy based on optimizing the number of samples at each k-space location based on the local amplitude of cardiac-induced signal instabilities.[49] The scan time increase is also comparable between both methods (12% vs 14%). However for ISME, this scan time increase is due to the diagonal pattern used to traverse the k-TE space of the data, which imposes a k-space boundary beyond that determined from the image encoding parameters. The use of advanced trajectories such as Gilbert curves might alleviate any scan time increase.[47,48] Also, ISME acts on all k-space frequencies of the data and might better mitigate spatially localized effects of cardiac pulsation.

With both standard multi-echo trajectories and ISME, neighbouring k-space data are acquired at different phases of the cardiac cycle. Therefore, individual echo images display spatial aliasing of pulsating MR signal across the field of view of the image. However, for the standard multi-echo trajectory, this aliasing is unchanged between echo images and the R_2* maps computed from the multi-echo data also exhibit aliasing. With the proposed ISME approach, aliasing artifacts vary across individual echo images because the phase of the cardiac cycle between neighbouring k-space indexes varies between images. As a result, spatial aliasing of pulsating MRI signal arising from e.g. arterial vessels is strongly reduced in R_2* maps. In the venous system, blood flow is largely constant and a dedicated flow-compensation technique should be preferred.[15] We highlight that ISME can be combined with flow-compensation techniques[15,82] or navigator-based corrections of breathing effects,[83,84] which were not used in this study.

With standard multi-echo trajectories, cardiac pulsation induces exponential-like effects on the decay of the multi-echo data that depends on the phase of cardiac cycle at the time of acquisition of the data. ISME allows the incoherent sampling of cardiac-induced signal instabilities in the multi-echo data, leading to a 13-18% increase in RMSE compared to standard multi-echo trajectories. Note that the higher RMSE with ISME does not imply that the effective noise level is higher: with ISME, the RMSE measures also include cardiac-induced effects that only manifest in the variability of R_2* and χ maps with standard multi-echo trajectories. ISME also leads to a more pronounced increase of the residuals with increasing echo time. To address this, we introduced a novel nonlinear weighted least squares (NWLS) approach for the estimation of R_2*, in which the weights are computed from the noise level of individual echo images using restricted maximum-likelihood (ReML), a statistical method that allows the modelling of noise heteroscedasticity within a dataset. ReML has found multiple applications in neuroimaging, in which noise has different physiological origins, such as the modelling of time correlations in functional MRI time series,[77] the modelling of motion-induced effects[74,85] or of non-uniform error variances in group-level analyses.[86] The proposed NWLS approach improves the distribution of the residuals across echoes, although a coherent pattern remains, and brings in an additional small reduction in variability of R_2* across repetitions (1-3%). This approach may bring more pronounced benefits with more complex models of transverse relaxation,[73,87] longer echo times or higher field strengths (e.g. 7T). Combined, the proposed ISME approach and NWLS estimation might allow the data to better comply with the requirements of independent and identically distributed noise for the denoising of multi-echo data.[88,89] Here, analysis of the RMSE and estimation using the proposed weighted least square approach was not conducted for χ as we only had access to compiled code for the estimation for this MRI parameter.

The proposed ISME method is a passive mitigation strategy which in effect averages out physiology-induced signal instabilities across the multiple echoes of the GRE data. Breathing induces periodic fluctuations of the main magnetic field B_0 in the head due to changes of the air volume in the

lungs.[16,35,90,91] The multi-echo data is acquired for different phases of the breathing cycle as well as cardiac cycle. Therefore, ISME acts on instabilities that arise from both cardiac pulsation[18] and breathing,[16,83,84] as long as these instabilities exhibit a semi-periodic behaviour.[47] The 20-25% reduction of R_2* variability with ISME is lower than recent estimates of cardiac-induced R_2* change (~35%),[18] presumably due to the higher image resolution. While this study drew its motivation from the effect of cardiac pulsation alone, it is likely that the reduction of R_2* and χ variability with ISME also arises from the mitigation of breathing-induced effects. Breathing has been identified as a dominant source of signal instabilities, albeit at longer echo times than the present study.[16,83,84]

The key novel aspect of ISME is the acquisition of multi-echo data at different phases of the cardiac cycle. The benefits of ISME were demonstrated using a simple GRE sequence as a starting point, for which the multi-echo data are acquired at a single k-space frequency after each RF excitation. Alternative strategies such as EPTI[53,54] or segmented EPI[55,56] have been introduced that allow dramatic scan time reductions and maintain a dense sampling of the MRI signal across echo times. These strategies divide k-space into segments that are sampled between consecutive shots. With the current implementations of these techniques, the multi-echo data of a given segment is acquired within a single shot. Because the shot-to-shot interval (TR) is typically shorter than the cardiac period, we expect the multi-echo data from one segment to be equally sensitive to cardiac-induced instabilities as the GRE sequence of the current work. Keeping the k-space filling pattern unchanged, implementation of ISME into EPTI or segmented EPI sequences would involve the generalization of spatial scrambling methods[47,48] to the additional dimension of the echo time, so that the multi-echo data of each segment is acquired across different phases of physiological cycles.

ISME shifts the current value of the k-space index between each readout of the multi-echo train. The k-space index is independent of the physical coordinates of the k-space data, and ISME is readily transferable to most sampling trajectories. Here we implemented ISME in a linear Cartesian trajectory. However, a pseudo-spiral trajectory has been used recently to reduce the level of cardiac-induced signal instabilities by increasing the number of samples near the k-space centre.[49] The combination of these two strategies could be beneficial e.g. when too few echo images are acquired to effectively sample the cardiac cycle between echoes with ISME alone ($N_{echoes} < 7$ from the present results). However, hardware limitations (amplitude, slew rate,…) might impose limits on the gradients required to shift the k-space index between the readouts. The impact of the eddy currents induced by these gradients on image quality should be carefully considered and might pose a practical limitation on the implementation of ISME in alternative sampling trajectories.

5. Conclusion

In this work, we proposed a new sampling strategy that reduce the effect of cardiac pulsation on estimates of the transverse relaxation rate (R_2*) and magnetic susceptibility (χ) computed from multi-echo gradient-echo data. The proposed sampling strategy, termed Incoherent Sampling of Multi-Echo data (ISME), is based on shifting the k-space position of the acquired data between each readout of the multi-echo train. With ISME, the multi-echo data is made up of points acquired at different phases of the cardiac cycle. As a result, the variability of R_2*/ χ maps across repetitions is reduced by 20-25% / 23-32% compared to standard multi-echo trajectories. With ISME, the spatial aliasing of pulsating MR signal is incoherent across the set of multi-echo images. This allows effective reduction of this aliasing in the R_2* maps computed from the data.

MRI data acquired with ISME show a stronger increase of the residual level with echo time. We introduce a novel nonlinear weighted-least squares (NWLS) approach for the computation of R_2* maps,

in which the weights are computed from the noise covariance matrix of the data – estimated using Restricted Maximum Likelihood. The proposed NWLS approach improves the distribution of the residuals across echo times.

ISME allows the effective reduction of cardiac-induced signal instabilities in in vivo gradient-echo data and enhances the sensitivity of R_2* and χ estimates to brain change in neuroscience studies.

Data availability statement

The high-resolution dataset is available online here (10.5281/zenodo.13364051). The Matlab code used for the estimation of the image-specific weights is available online here (10.5281/zenodo.14808609).

Funding information

This work was supported by the Swiss National Science Foundation (grant no 320030_184784 (AL); 32003B_182615 (RBvH) and CRSII5_202276 (RBvH)).

Ethics approval statement

This study received approval from the local Ethics Committee and all participants gave their written informed consent prior to participation.

6. Figures

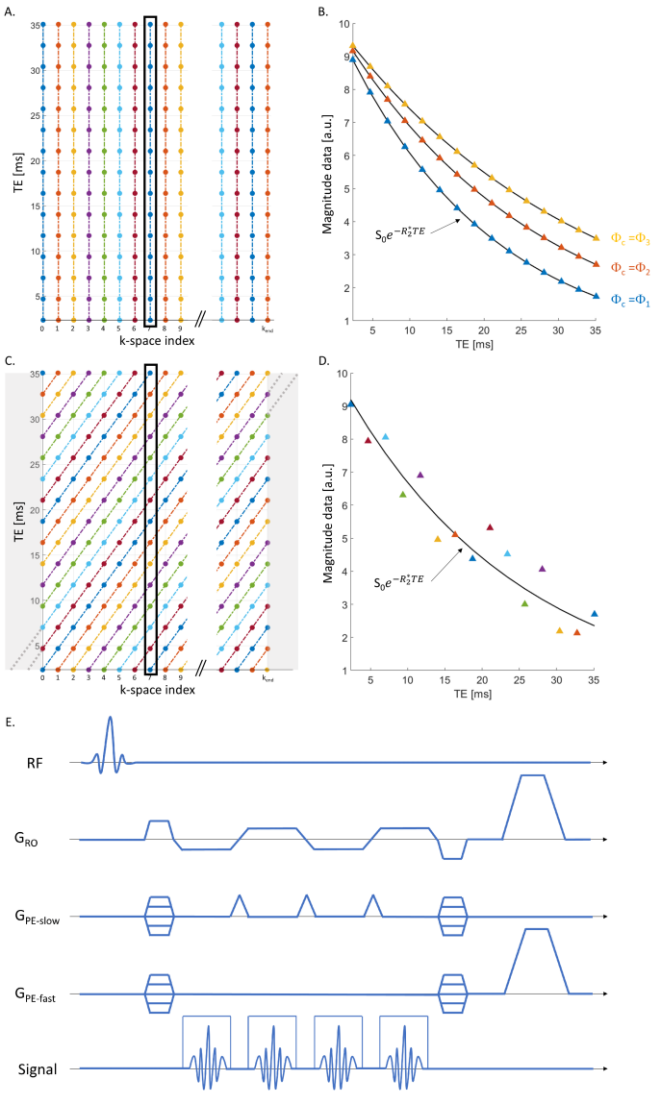

Figure 1: Traversal of the k-TE space with a standard multi-echo trajectory and with ISME. (A) The different colours represent different phases of the cardiac cycle. With a standard multi-echo trajectory, multi-echo data is acquired at a distinct k-space frequency following each radio-frequency excitation. Because the repetition time is much smaller than the cardiac period (TR $\lesssim$ 50ms), the multi-echo data at each k-space frequency is effectively acquired at the same phase of the cardiac cycle. (B) This multi-echo data contains exponential-like effects of cardiac pulsation on signal decay that depend on the phase of the cardiac cycle at the time of acquisition of the data. (C) To minimize the effect of cardiac pulsation on R_2* estimates, the proposed ISME strategy shifts the current value of the k-space index between the readouts of the multi-echo train. (D) As a result, the multi-echo data of each k-space location is made up of points acquired at different phases of the cardiac cycle. (E) Pulse diagram of the ISME GRE sequence. With ISME, the shift of the k-space index is implemented by means of short gradient pulses along the slow phase-encode direction (PE), as in EPI. However, unlike EPI, the data from the consecutive readouts of the multi-echo train are stored separately to obtain an individual image at each echo time.

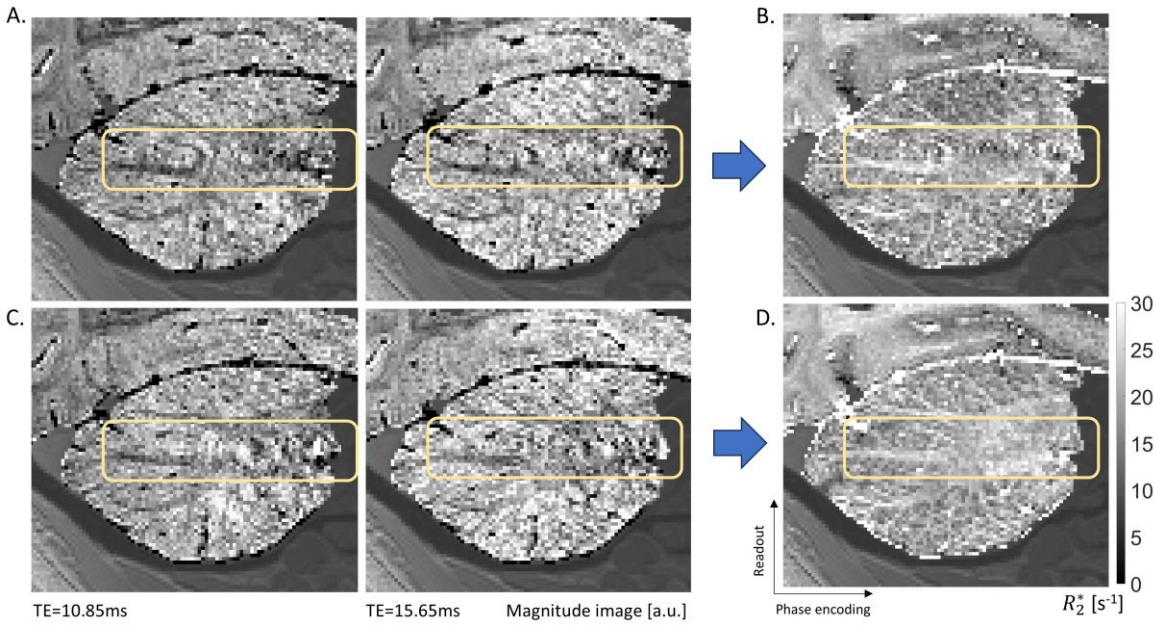

Figure 2: Example GRE images and corresponding R_2* maps (scanning protocol 2). (A) GRE images acquired with the standard multi-echo trajectory (TE = 10.85 ms and 15.65ms). (B) Corresponding R_2* map computed from the signal decay across echoes. (C) GRE images acquired with ISME (TE = 10.85 ms and 15.65ms). (D) Corresponding R_2* map computed from the signal decay across echoes. The light yellow rectangles highlight aliasing of pulsating signal originating from the nearby carotid artery, visible on the individual GRE images and the R_2* map computed from the data acquired with the standard multi-echo trajectory. This aliasing is not apparent in the R_2* map computed from the data acquired with ISME.

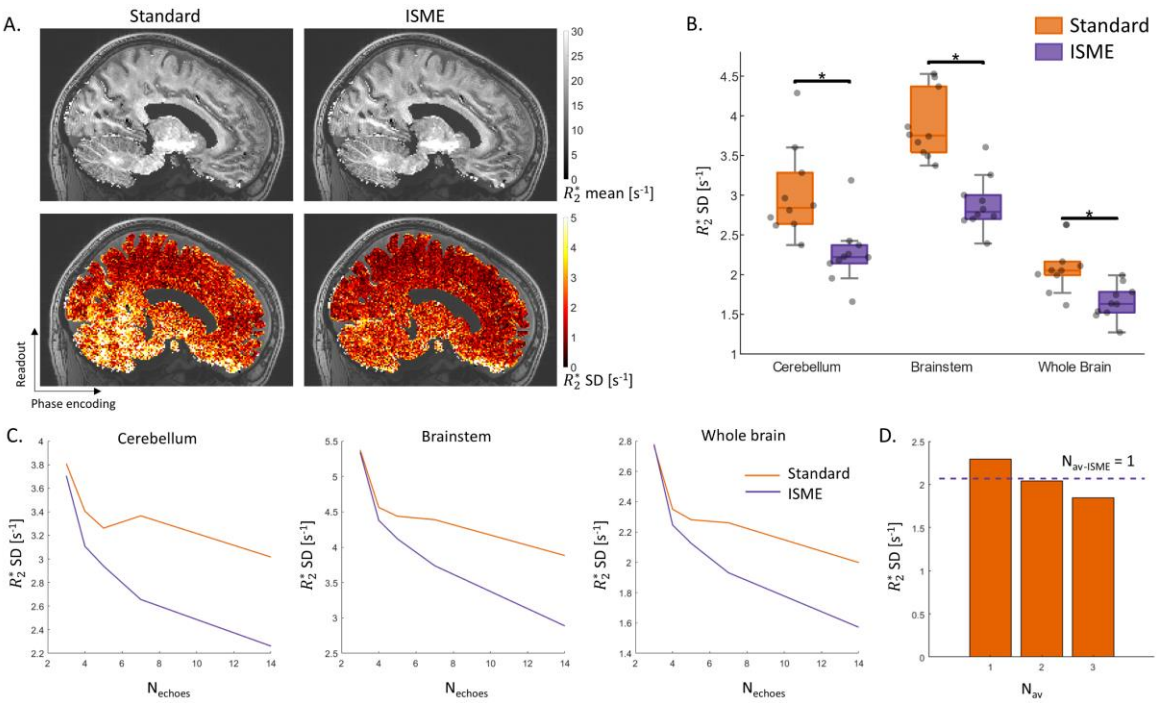

Figure 3: Mean and SD of R_2* across repetitions (scanning protocol 1). (A) Example mean and SD across repetitions of R_2* maps computed from data acquired with the standard multi-echo trajectory and ISME. (B) ROI-averaged SD of R_2* in the cerebellum, brainstem and whole brain for each subject, computed from data acquired with the standard multi-echo trajectory and ISME. (C) Whole-brain average of the SD across repetitions of R_2* maps computed from an increasing number of echo images (N_{echoes}). (D) Average SD across repetitions of R_2* maps computed from N_{av}=1, 2, and 3 datasets acquired with the standard multi-echo trajectory and from $N_{av\text{-}ISME}$=1 dataset acquired with ISME (N_{echoes}=14). (A-C) were computed from the data acquired in experiment 1. (D) was computed from the data acquired in experiment 2.

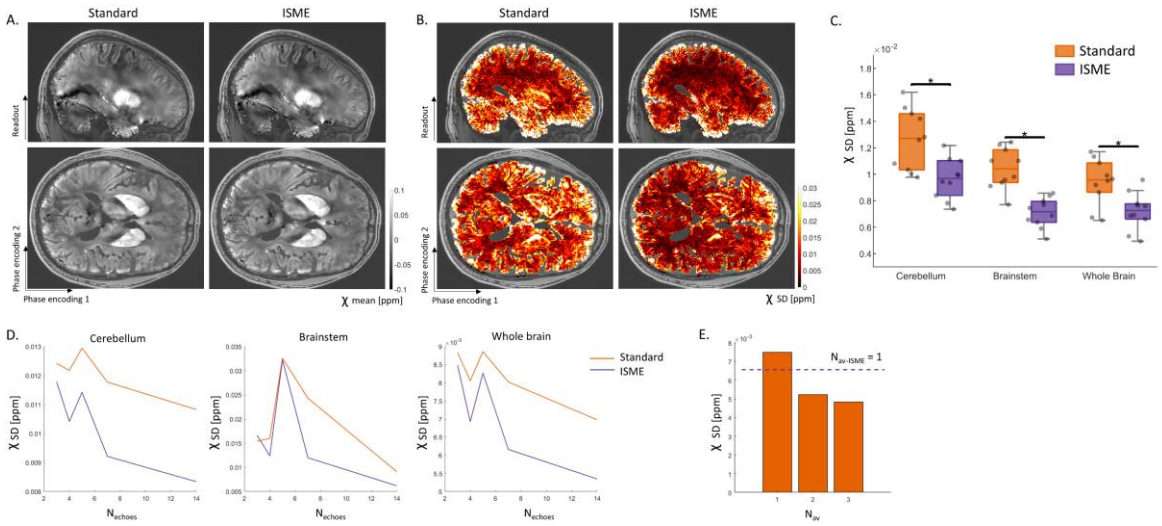

Figure 4: Mean and SD of magnetic susceptibility (χ) across repetitions (scanning protocol 1). Example mean (A) and SD (B) across repetitions of χ maps computed from data acquired with the standard multi-echo trajectory and ISME. (C) ROI-averaged SD of χ estimates in the cerebellum, brainstem and whole brain for each subject, computed from data acquired with the standard multi-echo trajectory and ISME. (D) Whole-brain average of the SD across repetitions of χ maps computed from an increasing number of echo images (N_{echoes}). (E) Average SD across repetitions of χ maps computed from N_{av}=1, 2, and 3 datasets acquired with the standard multi-echo trajectory and from $N_{av\text{-}ISME}$=1 dataset acquired with ISME (N_{echoes}=14). (A-D) were computed from the data acquired in experiment 1. (E) was computed from the data acquired in experiment 2.

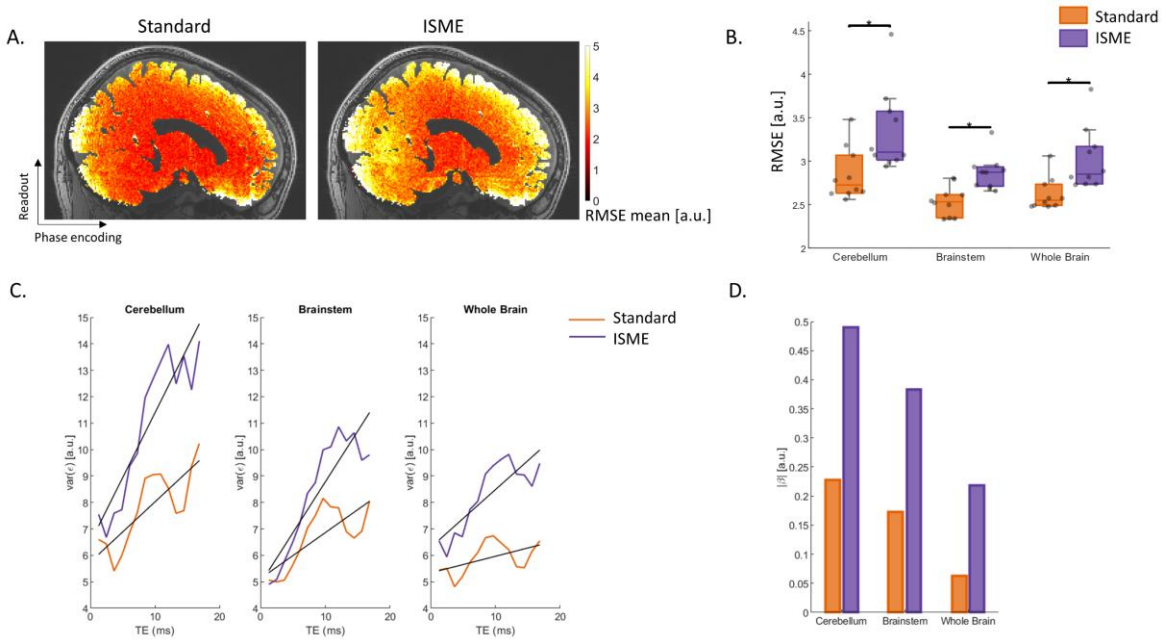

Figure 5: Lack of fit of the R_2* estimates (scanning protocol 1, experiment 1). (A) Example map of the mean root mean square error (RMSE) of R_2* fits across repetitions, computed from data acquired with a standard multi-echo trajectory and with ISME. (B) Regional RMSE levels in the cerebellum, brainstem and whole brain. (C) Variance of the residuals (ε) across repetitions as a function of echo time for both the standard multi-echo trajectory (orange) and ISME (purple). (D) Rate of increase of the variance of the residuals with the echo time.

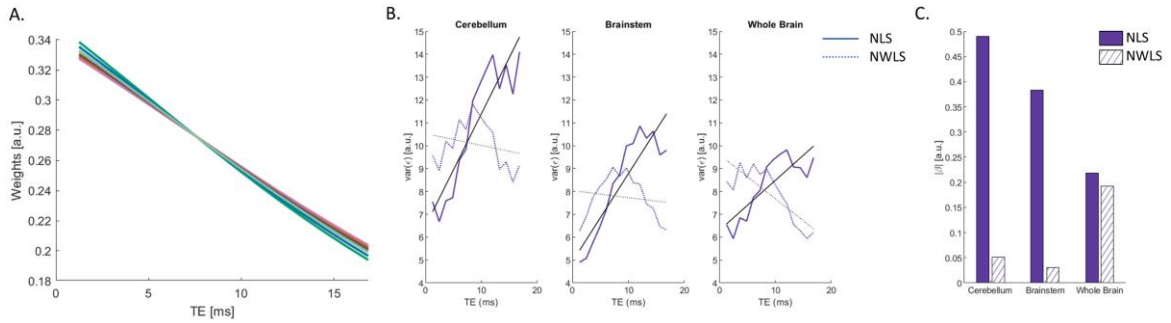

Figure 6: Lack of fit of the R_2* estimates with the proposed NWLS approach (scanning protocol 1, experiment 1). (A) Weights computed with the proposed NWLS approach for each study participant. (B) Variance of the residuals (ε) across repetitions as a function of echo time, following estimation of R_2* from the ISME data with the NLS and the NWLS approaches (B). (C) Rate of increase of the variance of the residuals with the echo time with the NLS and the NWLS approaches.

7. Tables

	TR	TE	Resolution	Tilt	Duration	# repetitions
Protocol 1	21ms	TE_{min}=1.25ms; echo spacing = 1.2ms	$(1.2\ mm)^3$	30°	5:29 (Standard) 6:08 (ISME)	Experiment 1: 3 (Standard); 3 (ISME) Experiment 2: 9 (Standard); 3 (ISME)
Protocol 2	35.55ms	TE_{min}=2.3ms; echo spacing = 2.14ms spacing	$(0.8\ mm)^3$	0°	18:52 (Standard) 20:28 (ISME)	1

Table 1: Scanning protocols.

	R_2* SD [s^{-1}]			RMSE [a.u.]			χ SD [ppb]	
	Standard	ISME NLS	ISME NWLS	Standard	ISME NLS	ISME NWLS	Standard	ISME
Brainstem	3.02±0.57	2.26±0.39	2.20±0.35	2.85±0.30	3.34±0.48	3.27±0.43	12.63±2.32	9.66±1.52
Cerebellum	3.88±0.43	2.89±0.34	2.83±0.29	2.54±0.17	2.86±0.20	2.77±0.18	10.41±1.54	7.09±1.12
Whole brain	2.00±0.31	1.57±0.20	1.56±0.20	2.58±0.19	2.97±0.36	2.95±0.34	8.72±1.67	6.57±1.31
Occipital lobe	1.99±0.40	1.64±0.30	1.60±0.29	3.03±0.26	3.42±0.43	3.41±0.37	12.52±3.53	10.23±2.67
Frontal lobe	1.77±0.38	1.46±0.28	1.47±0.28	2.70±0.24	3.17±0.50	3.19±0.50	9.99±1.95	7.87±2.11
Parietal lobe	1.65±0.27	1.39±0.21	1.39±0.21	2.70±0.17	3.08±0.34	3.12±0.32	10.07±2.25	8.05±1.51
Temporal lobe	2.24±0.35	1.78±0.27	1.73±0.26	2.63±0.20	3.11±0.40	3.06±0.35	9.36±2.18	6.73±1.81
Corticospinal tract	2.38±0.28	1.85±0.22	1.84±0.20	2.39±0.12	2.66±0.24	2.63±0.22	7.44±1.29	5.32±0.97
Inferior Longitudinal Fasciculus	2.24±0.41	1.68±0.35	1.65±0.23	2.28±0.21	2.78±0.36	2.72±0.31	7.58±1.64	5.43±1.49
Optic radiation	1.63±0.31	1.30±0.20	1.28±0.18	2.64±0.29	2.98±0.44	2.95±0.39	6.86±1.97	5.10±1.32

Table 2: Variability of R_2* estimates across repetitions, lack of fit of the R_2* estimates (RMSE) and variability of magnetic susceptibility (χ) estimates across repetitions, from data acquired with a

standard multi-echo trajectories and with ISME. For the data acquired with ISME, the R_2* variability and RMSE estimates were computed using nonlinear least squares (NLS) and nonlinear weighted least squares (NWLS).

8. Reference

1. Cohen-Adad J. What can we learn from T2* maps of the cortex? *NeuroImage*. 2014;93:189-200. doi:10.1016/j.neuroimage.2013.01.023

2. Deistung A, Schweser F, Reichenbach JR. Overview of quantitative susceptibility mapping. *NMR in Biomedicine*. 2017;30(4). doi:10.1002/nbm.3569

3. Fukunaga M, Li TQ, Van Gelderen P, et al. Layer-specific variation of iron content in cerebral cortex as a source of MRI contrast. *Proceedings of the National Academy of Sciences of the United States of America*. 2010;107(8):3834-3839. doi:10.1073/pnas.0911177107

4. Stüber C, Morawski M, Schäfer A, et al. Myelin and iron concentration in the human brain: A quantitative study of MRI contrast. *NeuroImage*. 2014;93(P1):95-106. doi:10.1016/j.neuroimage.2014.02.026

5. Langkammer C, Ropele S, Pirpamer L, Fazekas F, Schmidt R. MRI for iron mapping in Alzheimer's disease. *Neurodegenerative Diseases*. 2014;13(2-3):189-191. doi:10.1159/000353756

6. Ulla M, Bonny JM, Ouchchane L, Rieu I, Claise B, Durif F. Is R2* a New MRI Biomarker for the Progression of Parkinson's Disease? A Longitudinal Follow-Up. *PLoS ONE*. 2013;8(3). doi:10.1371/journal.pone.0057904

7. Ghadery C, Pirpamer L, Hofer E, et al. R2* mapping for brain iron: Associations with cognition in normal aging. *Neurobiology of Aging*. 2015;36(2):925-932. doi:10.1016/j.neurobiolaging.2014.09.013

8. Roemer PB, Edelstein WA, Hayes CE, Souza SP, Mueller OM. The NMR phased array. *Magnetic Resonance in Medicine*. 1990;16(2):192-225. doi:10.1002/mrm.1910160203

9. Constantinides CD, Atalar E, McVeigh ER. Signal-to-noise measurements in magnitude images from NMR phased arrays. *Magnetic Resonance in Medicine*. 1997;38(5):852-857. doi:10.1002/mrm.1910380524

10. Triantafyllou C, Polimeni JR, Wald LL. Physiological noise and signal-to-noise ratio in fMRI with multi-channel array coils. *NeuroImage*. 2011;55(2):597-606. doi:10.1016/j.neuroimage.2010.11.084

11. Krüger G, Glover GH. Physiological noise in oxygenation-sensitive magnetic resonance imaging. *Magnetic Resonance in Medicine*. 2001;46(4):631-637. doi:10.1002/mrm.1240

12. Glover GH, Li TQ, Ress D. Image-based method for retrospective correction of physiological motion effects in fMRI: RETROICOR. *Magnetic Resonance in Medicine*. 2000;44(1):162-167. doi:10.1002/1522-2594(200007)44:1<162::AID-MRM23>3.0.CO;2-E

13. Birn RM, Diamond JB, Smith MA, Bandettini PA. Separating respiratory-variation-related fluctuations from neuronal-activity-related fluctuations in fMRI. *NeuroImage*. 2006;31(4):1536-1548. doi:10.1016/j.neuroimage.2006.02.048

14. Raj D, Paey DP, Anderson AW, Kennan RP, Gore JC. A model for susceptibility artefacts from respiration in functional echo-planar magnetic resonance imaging. *Physics in Medicine and Biology*. 2000;45(12):3809-3820. doi:10.1088/0031-9155/45/12/321

15. Xu B, Liu T, Spincemaille P, Prince M, Wang Y. Flow compensated quantitative susceptibility mapping for venous oxygenation imaging. *Magnetic Resonance in Medicine*. 2014;72(2):438-445. doi:10.1002/mrm.24937

16. Choi JY, Lee J, Nam Y, Lee J, Oh SH. Improvement of reproducibility in quantitative susceptibility mapping (QSM) and transverse relaxation rates (R2*) after physiological noise correction. *Journal of Magnetic Resonance Imaging*. 2019;49(6):1769-1776. doi:10.1002/jmri.26522

17. Khalil M, Enzinger C, Langkammer C, et al. Quantitative assessment of brain iron by R2* relaxometry in patients with clinically isolated syndrome and relapsing-remitting multiple sclerosis. *Multiple Sclerosis*. 2009;15(9):1048-1054. doi:10.1177/1352458509106609

18. Raynaud Q, Di Domenicantonio G, Yerly J, Dardano T, van Heeswijk RB, Lutti A. A characterization of cardiac-induced noise in R2* maps of the brain. *Magnetic Resonance in Medicine*. 2024;91(1):237-251. doi:10.1002/mrm.29853

19. Windischberger C, Langenberger H, Sycha T, et al. On the origin of respiratory artifacts in BOLD-EPI of the human brain. *Magnetic Resonance Imaging*. 2002;20(8):575-582. doi:10.1016/S0730-725X(02)00563-5

20. Maclaren J, Armstrong BSR, Barrows RT, et al. Measurement and Correction of Microscopic Head Motion during Magnetic Resonance Imaging of the Brain. *PLoS ONE*. 2012;7(11). doi:10.1371/journal.pone.0048088

21. Chen L, Beckett A, Verma A, Feinberg DA. Dynamics of respiratory and cardiac CSF motion revealed with real-time simultaneous multi-slice EPI velocity phase contrast imaging. *NeuroImage*. 2015;122:281-287. doi:10.1016/j.neuroimage.2015.07.073

22. Hermes D, Wu H, Kerr AB, Wandell BA. Measuring brain beats: Cardiac-aligned fast functional magnetic resonance imaging signals. *Human Brain Mapping*. 2023;44(1):280-294. doi:10.1002/hbm.26128

23. Sloots JJ, Froeling M, Biessels GJ, Zwanenburg JJM. Dynamic brain ADC variations over the cardiac cycle and their relation to tissue strain assessed with DENSE at high-field MRI. *Magnetic Resonance in Medicine*. 2022;88(1):266-279. doi:10.1002/mrm.29209

24. Adams AL, Viergever MA, Luijten PR, Zwanenburg JJM. Validating faster DENSE measurements of cardiac-induced brain tissue expansion as a potential tool for investigating cerebral microvascular pulsations. *NeuroImage*. 2020;208. doi:10.1016/j.neuroimage.2019.116466

25. Brooks JCW, Faull OK, Pattinson KTS, Jenkinson M. Physiological noise in brainstem fMRI. *Frontiers in Human Neuroscience*. 2013;(OCT). doi:10.3389/fnhum.2013.00623

26. Beissner F. Functional MRI of the Brainstem: Common Problems and their Solutions. *Clinical Neuroradiology*. 2015;25:251-257. doi:10.1007/s00062-015-0404-0

27. van der Zwaag W, Jorge J, Butticaz D, Gruetter R. Physiological noise in human cerebellar fMRI. *Magnetic Resonance Materials in Physics, Biology and Medicine*. 2015;28(5):485-492. doi:10.1007/s10334-015-0483-6

28. Bianciardi M, Toschi N, Polimeni JR, et al. The pulsatility volume index: An indicator of cerebrovascular compliance based on fast magnetic resonance imaging of cardiac and respiratory pulsatility. *Philosophical Transactions of the Royal Society A: Mathematical, Physical and Engineering Sciences*. 2016;374(2067). doi:10.1098/rsta.2015.0184

29. Morgan AG, Thrippleton MJ, Wardlaw JM, Marshall I. 4D flow MRI for non-invasive measurement of blood flow in the brain: A systematic review. *Journal of Cerebral Blood Flow and Metabolism*. 2021;41(2):206-218. doi:10.1177/0271678X20952014

30. Schuchardt F, Schroeder L, Anastasopoulos C, et al. In vivo analysis of physiological 3D blood flow of cerebral veins. *European Radiology*. 2015;25(8):2371-2380. doi:10.1007/s00330-014-3587-x

31. Petridou N, Schäfer A, Gowland P, Bowtell R. Phase vs. magnitude information in functional magnetic resonance imaging time series: toward understanding the noise. *Magnetic Resonance Imaging*. 2009;27(8):1046-1057. doi:10.1016/j.mri.2009.02.006

32. Menon RS. Postacquisition suppression of large-vessel BOLD signals in high-resolution fMRI. *Magnetic Resonance in Medicine*. 2002;47(1):1-9. doi:10.1002/mrm.10041

33. Dagli MS, Ingeholm JE, Haxby JV. Localization of cardiac-induced signal change in fMRI. *NeuroImage*. 1999;9(4):407-415. doi:10.1006/nimg.1998.0424

34. Deckers RHR, van Gelderen P, Ries M, et al. An adaptive filter for suppression of cardiac and respiratory noise in MRI time series data. *NeuroImage*. 2006;33(4):1072-1081. doi:10.1016/j.neuroimage.2006.08.006

35. Gelderen P van, Zwart JA de, Starewicz P, Hinks RS, Duyn JH. Real-Time Shimming to Compensate for Respiration- Induced B0 Fluctuations. *Magnetic Resonance in Medicine*. Published online 2007.

36. Larson TC, Kelly WM, Ehman RL, Wehrli FW. Spatial misregistration of vascular flow during MR imaging of the CNS: Cause and clinical significance. *American Journal of Neuroradiology*. 1990;11(5):1041-1048.

37. Wymer DT, Patel KP, Burke WF, Bhatia VK. Phase-contrast MRI: Physics, techniques, and clinical applications. *Radiographics*. 2020;40(1):122-140. doi:10.1148/rg.2020190039

38. Godenschweger F, Kägebein U, Stucht D, et al. Motion correction in MRI of the brain. *Physics in Medicine and Biology*. 2016;61(5):R32-R56. doi:10.1088/0031-9155/61/5/R32

39. Welch EB, Felmlee JP, Ehman RL, Manduca A. Motion correction using the k-space phase difference of orthogonal acquisitions. *Magnetic Resonance in Medicine*. 2002;48(1):147-156. doi:10.1002/mrm.10179

40. Zaitsev M, Maclaren J, Herbst M. Motion artifacts in MRI: A complex problem with many partial solutions. *Journal of Magnetic Resonance Imaging*. 2015;42(4):887-901. doi:10.1002/jmri.24850

41. Borup DD, Elkins CJ, Eaton JK. Effects of motion on MRI signal decay from micron-scale particles. *Journal of Magnetic Resonance*. 2019;305:152-161. doi:10.1016/j.jmr.2019.06.014

42. Yang X, Sammet S, Schmalbrock P, Knopp MV. Postprocessing correction for distortions in T2 decay caused by quadratic cross-Slice B0 inhomogeneity. *Magnetic Resonance in Medicine*. 2010;63(5):1258-1268. doi:10.1002/mrm.22316

43. Agrawal U, Brown EN, Lewis LD. Model-based physiological noise removal in fast fMRI. *NeuroImage*. 2020;205. doi:10.1016/j.neuroimage.2019.116231

44. Tijssen RHN, Jenkinson M, Brooks JCW, Jezzard P, Miller KL. Optimizing RetroICor and RetroKCor corrections for multi-shot 3D FMRI acquisitions. *NeuroImage*. 2014;84:394-405. doi:10.1016/j.neuroimage.2013.08.062

45. Wallace TE, Kober T, Stockmann JP, Polimeni JR, Warfield SK, Afacan O. Real-time shimming with FID navigators. *Magnetic Resonance in Medicine*. 2022;88(6):2548-2563. doi:10.1002/mrm.29421

46. Wallace TE, Polimeni JR, Stockmann JP, et al. Dynamic distortion correction for functional MRI using FID navigators. *Magnetic Resonance in Medicine*. 2021;85(3):1294-1307. doi:10.1002/mrm.28505

47. Seginer A, Schmidt R. Messing up to clean up: Semi-randomized frequency selective space-filling curves to suppress physiological signal fluctuations in MRI. *Magnetic Resonance in Medicine*. 2023;90(6):2275-2289. doi:10.1002/mrm.29790

48. Seginer A, Niry D, Furman-Haran E, Kolb H, Schmidt R. Reducing blood flow pulsation artifacts in 3D time-of-flight angiography by locally scrambling the order of the acquisition at 3 T and 7 T. *Magnetic Resonance in Medicine*. Published online 2024. doi:10.1002/mrm.30196

49. Raynaud Q, Dardano T, Oliveira R, et al. Data acquisition strategies to reduce cardiac-induced noise in brain maps of R 2 * and magnetic susceptibility. *bioRxiv*. Published online 2024. doi:10.1101/2024.08.20.608759

50. Mansfield P. Multi-planar image formation using NMR spin echoes. *Journal of Physics C: Solid State Physics*. 1977;10(3):L55. doi:10.1088/0022-3719/10/3/004

51. Griswold MA, Jakob PM, Heidemann RM, et al. Generalized Autocalibrating Partially Parallel Acquisitions (GRAPPA). *Magnetic Resonance in Medicine*. 2002;47(6):1202-1210. doi:10.1002/mrm.10171

52. Breuer FA, Blaimer M, Mueller MF, et al. Controlled aliasing in volumetric parallel imaging (2D CAIPIRINHA). *Magnetic Resonance in Medicine*. 2006;55(3):549-556. doi:10.1002/mrm.20787

53. Wang F, Dong Z, Reese TG, Rosen B, Wald LL, Setsompop K. 3D Echo Planar Time-resolved Imaging (3D-EPTI) for ultrafast multi-parametric quantitative MRI. *NeuroImage*. 2022;250. doi:10.1016/j.neuroimage.2022.118963

54. Wang F, Dong Z, Reese TG, et al. Echo planar time-resolved imaging (EPTI). *Magnetic Resonance in Medicine*. 2019;81(6):3599-3615. doi:10.1002/mrm.27673

55. Stirnberg R, Deistung A, Reichenbach JR, Breteler MMB, Stöcker T. Rapid submillimeter QSM and R2* mapping using interleaved multishot 3D-EPI at 7 and 3 Tesla. *Magnetic Resonance in Medicine*. Published online December 2024. doi:10.1002/mrm.30216

56. Zwanenburg JJM, Versluis MJ, Luijten PR, Petridou N. Fast high resolution whole brain T2* weighted imaging using echo planar imaging at 7T. *NeuroImage*. 2011;56(4):1902-1907. doi:10.1016/j.neuroimage.2011.03.046

57. Benner T, Jellus V, Wang R, et al. *Adaptive Combination of Phased Array Signals for Diffusion Imaging*.; 2017. https://www.researchgate.net/publication/265808112

58. Walsh DO, Gmitro AF, Marcellin MW. Adaptive reconstruction of phased array MR imagery. *Magnetic Resonance in Medicine*. 2000;43(5):682-690. doi:10.1002/(SICI)1522-2594(200005)43:5<682::AID-MRM10>3.0.CO;2-G

59. Eckstein K, Dymerska B, Bachrata B, et al. Computationally Efficient Combination of Multi-channel Phase Data From Multi-echo Acquisitions (ASPIRE). *Magnetic Resonance in Medicine*. 2018;79(6):2996-3006. doi:10.1002/mrm.26963

60. Lutti A, Hutton C, Finsterbusch J, Helms G, Weiskopf N. Optimization and validation of methods for mapping of the radiofrequency transmit field at 3T. *Magnetic Resonance in Medicine*. 2010;64(1):229-238. doi:10.1002/mrm.22421

61. Lutti A, Stadler J, Josephs O, et al. Robust and fast whole brain mapping of the RF transmit field B1 at 7T. *PLoS ONE*. 2012;7(3). doi:10.1371/journal.pone.0032379

62. Helms G, Dathe H, Kallenberg K, Dechent P. High-resolution maps of magnetization transfer with inherent correction for RF inhomogeneity and T1 relaxation obtained from 3D FLASH MRI. *Magnetic Resonance in Medicine*. 2008;60(6):1396-1407. doi:10.1002/mrm.21732

63. Tabelow K, Balteau E, Ashburner J, et al. hMRI – A toolbox for quantitative MRI in neuroscience and clinical research. *NeuroImage*. 2019;194:191-210. doi:10.1016/j.neuroimage.2019.01.029

64. Helms G, Draganski B, Frackowiak R, Ashburner J, Weiskopf N. Improved segmentation of deep brain grey matter structures using magnetization transfer (MT) parameter maps. *NeuroImage*. 2009;47(1):194-198. doi:10.1016/j.neuroimage.2009.03.053

65. Weiskopf N, Suckling J, Williams G, et al. Quantitative multi-parameter mapping of R1, PD*, MT, and R2* at 3T: A multi-center validation. *Frontiers in Neuroscience*. 2013;(7 JUN). doi:10.3389/fnins.2013.00095

66. Ashburner J, Friston KJ. Unified segmentation. *NeuroImage*. 2005;26(3):839-851. doi:10.1016/j.neuroimage.2005.02.018

67. Weiskopf N, Hutton C, Josephs O, Turner R, Deichmann R. Optimized EPI for fMRI studies of the orbitofrontal cortex: Compensation of susceptibility-induced gradients in the readout direction. *Magnetic Resonance Materials in Physics, Biology and Medicine*. 2007;20(1):39-49. doi:10.1007/s10334-006-0067-6

68. Mori S, Wakana S, Van Zijl PC, Nagae-Poetscher L. *MRI Atlas of Human White Matter*. Elsevier; 2005.

69. Wakana S, Caprihan A, Panzenboeck MM, et al. Reproducibility of quantitative tractography methods applied to cerebral white matter. *NeuroImage*. 2007;36(3):630-644. doi:10.1016/j.neuroimage.2007.02.049

70. Hua K, Zhang J, Wakana S, et al. Tract probability maps in stereotaxic spaces: Analyses of white matter anatomy and tract-specific quantification. *NeuroImage*. 2008;39(1):336-347. doi:10.1016/j.neuroimage.2007.07.053

71. Veraart J, Novikov DS, Christiaens D, Ades-aron B, Sijbers J, Fieremans E. Denoising of diffusion MRI using random matrix theory. *NeuroImage*. 2016;142:394-406. doi:10.1016/j.neuroimage.2016.08.016

72. Schilling KG, Fadnavis S, Batson J, et al. Denoising of diffusion MRI in the cervical spinal cord – effects of denoising strategy and acquisition on intra-cord contrast, signal modeling, and feature conspicuity. *NeuroImage*. 2023;266. doi:10.1016/j.neuroimage.2022.119826

73. Oliveira R, Raynaud Q, Jelescu I, Kiselev VG, Kirilina E, Lutti A. In Vivo Characterization of Magnetic Inclusions in the Subcortex From Nonexponential Transverse Relaxation Decay. *NMR in Biomedicine*. 2025;38(6). doi:10.1002/nbm.70051

74. Lutti A, Corbin N, Ashburner J, et al. Restoring statistical validity in group analyses of motion-corrupted MRI data. *Human Brain Mapping*. 2022;43(6):1973-1983. doi:10.1002/hbm.25767

75. Corbin N, Oliveira R, Raynaud Q, et al. Statistical analyses of motion-corrupted MRI relaxometry data computed from multiple scans. *Journal of Neuroscience Methods*. 2023;398. doi:10.1016/j.jneumeth.2023.109950

76. Castella R, Arn L, Dupuis E, Callaghan MF, Draganski B, Lutti A. Controlling motion artefact levels in MR images by suspending data acquisition during periods of head motion. *Magnetic Resonance in Medicine*. 2018;80(6):2415-2426. doi:10.1002/mrm.27214

77. Friston KJ, Penny W, Phillips C, Kiebel S, Hinton G, Ashburner J. Classical and Bayesian inference in neuroimaging: Theory. *NeuroImage*. 2002;16(2):465-483. doi:10.1006/nimg.2002.1090

78. Dymerska B, Eckstein K, Bachrata B, et al. Phase unwrapping with a rapid opensource minimum spanning tree algorithm (ROMEO). *Magnetic Resonance in Medicine*. 2021;85(4):2294-2308. doi:10.1002/mrm.28563

79. Hu W, Liu H, Chen D, et al. Coil combination of multichannel single voxel magnetic resonance spectroscopy with repeatedly sampled in vivo data. *Molecules*. 2021;26(13). doi:10.3390/molecules26133896

80. Chan KS, Marques JP. SEPIA—Susceptibility mapping pipeline tool for phase images. *NeuroImage*. 2021;227. doi:10.1016/j.neuroimage.2020.117611

81. Wei H, Dibb R, Zhou Y, et al. Streaking artifact reduction for quantitative susceptibility mapping of sources with large dynamic range. *NMR in Biomedicine*. 2015;28(10):1294-1303. doi:10.1002/nbm.3383

82. Nam Y, Kim DH, Lee J. Physiological noise compensation in gradient-echo myelin water imaging. *NeuroImage*. 2015;120:345-349. doi:10.1016/j.neuroimage.2015.07.014

83. Versluis MJ, Peeters JM, van Rooden S, et al. Origin and reduction of motion and f0 artifacts in high resolution T2*-weighted magnetic resonance imaging: Application in Alzheimer's disease patients. *NeuroImage*. 2010;51(3):1082-1088. doi:10.1016/j.neuroimage.2010.03.048

84. Wen J, Cross AH, Yablonskiy DA. On the role of physiological fluctuations in quantitative gradient echo MRI: Implications for GEPCI, QSM, and SWI. *Magnetic Resonance in Medicine*. 2015;73(1):195-203. doi:10.1002/mrm.25114

85. Diedrichsen J, Shadmehr R. Detecting and adjusting for artifacts in fMRI time series data. *NeuroImage*. 2005;27(3):624-634. doi:10.1016/j.neuroimage.2005.04.039

86. Friston KJ, Stephan KE, Lund TE, Morcom A, Kiebel S. Mixed-effects and fMRI studies. *NeuroImage*. 2005;24(1):244-252. doi:10.1016/j.neuroimage.2004.08.055

87. Chan KS, Chamberland M, Marques JP. On the performance of multi-compartment relaxometry for myelin water imaging (MCR-MWI) – test-retest repeatability and inter-protocol reproducibility. *NeuroImage*. 2023;266. doi:10.1016/j.neuroimage.2022.119824

88. Does MD, Olesen JL, Harkins KD, et al. Evaluation of principal component analysis image denoising on multi-exponential MRI relaxometry. *Magnetic Resonance in Medicine*. 2019;81(6):3503-3514. doi:10.1002/mrm.27658

89. Bustin A, Lima da Cruz G, Jaubert O, Lopez K, Botnar RM, Prieto C. High-dimensionality undersampled patch-based reconstruction (HD-PROST) for accelerated multi-contrast MRI. *Magnetic Resonance in Medicine*. 2019;81(6):3705-3719. doi:10.1002/mrm.27694

90. Marques JP, Bowtell R. Application of a fourier-based method for rapid calculation of field inhomogeneity due to spatial variation of magnetic susceptibility. *Concepts in Magnetic Resonance Part B: Magnetic Resonance Engineering*. 2005;25(1):65-78. doi:10.1002/cmr.b.20034

91. Cheng H, Li Y. Respiratory noise correction using phase information. *Magnetic Resonance Imaging*. 2010;28(4):574-582. doi:10.1016/j.mri.2009.12.014

92. Budrys T, Veikutis V, Lukosevicius S, Gleizniene R, Monastyreckiene E, Kulakiene I. Artifacts in magnetic resonance imaging: How it can really affect diagnostic image quality and confuse clinical diagnosis? *Journal of Vibroengineering*. 2018;20(2):1202-1213. doi:10.21595/jve.2018.19756

93. Cavanaugh JE, Neath AA. The Akaike information criterion: Background, derivation, properties, application, interpretation, and refinements. *Wiley Interdisciplinary Reviews: Computational Statistics*. 2019;11(3). doi:10.1002/wics.1460

94. Chen WC, Foxley S, Miller KL. Detecting microstructural properties of white matter based on compartmentalization of magnetic susceptibility. *NeuroImage*. 2013;70:1-9. doi:10.1016/j.neuroimage.2012.12.032

1. Supplementary material

1.1. Motion degradation index

The index introduced in Castella et al. [74–76] was calculated from each multi-echo dataset to estimate the level of image degradation caused by head motion ('Motion Degradation Index', MDI). The distribution of MDI values peaked at MDI ~$3.5s^{-1}$, reflecting an overall high image quality (Figure S1). However, four datasets from the same subject exhibit MDI values above $4s^{-1}$, indicative of poor quality due to head motion. The data from this subject was removed from subsequent analyses.

1.2. Mitigation of eye movement artefacts

Eye movement during the acquisition of MRI data leads to image aliasing along the slow phase-encoding direction of a 3D-encoded image. When the slow phase-encoding direction is oriented along the anterior-posterior direction of the patient, this aliasing propagates across the brain with a standard multi-echo trajectory (Figure S2A). However, this aliasing artifact is largely mitigated with the proposed ISME approach (Figure S2B). To keep the focus of this study specifically on cardiac-induced effects, the imaging box was tilted by 30 degrees in the sagittal plane to displace this artefact below the brain.[92]

1.3. Model optimization for estimation of R2* using NWLS

Fitting a nonlinear model with a weighted LS approach involves two sets of unknowns: the model parameters and the weights, with the latter corresponding to the inverse of the variance of the residuals at each echo time. Estimating both sets of parameters by maximum-likelihood results in biased estimates of (co)variance, which in turn bias the estimated model parameters. In contrast, restricted maximum-likelihood approaches (ReML) yield unbiased estimates of variance. ReML, however, does not lend itself easily to nonlinear models. We therefore devised a two-step procedure, whereby a linear ReML estimate of variance is performed first using a Taylor expansion of the transverse signal decay, and the resulting weights are then used in a nonlinear weighted least square (NWLS) fit. ReML estimation was performed using the function `spm_reml` in SPM (the analysis script is provided with this article). The covariance matrix of the residual noise was assumed diagonal, with weights modelled as a polynomial in TE. As is standard in SPM, we assumed that this covariance matrix is shared across all voxels within a brain volume.

We identified the optimal order of the Taylor expansion (M) from the Akaike information criterion corrected for small sample size (AICc). The AICc rewards the goodness of fit and penalizes the number of estimated parameters.[93] The minimal values of the AICc were found for Taylor expansion orders of 1 and 2 (Figure S3A). We opted for a Taylor expansion of order M=2 to accommodate local deviations from the linear approximation of the signal decay due to e.g. high decay rate in iron-rich regions (pallidum, red nuclei, substantia nigra,..) or deviations from the exponential behaviour in white matter and sub-cortical areas.[73,87,94]

From the results of the NLS analyses shown in Figure 5C, models of the dependence of the residuals on the echo time of the data were assumed to follow a polynomial form of order N. Model selection was conducted from the estimates of the evidence lower bound (ELBO) provided by the implementation of ReML of the SPM software.[77] The ELBO favours the reduction of residual errors and penalises model complexity. An optimal noise model maximises the ELBO. Compared to N=0 (uniform residual level across echo times), the optimal noise model was found to be N=3 for data acquired with

the standard multi-echo trajectory. The corresponding increase in ELBO was ΔELBO=ELBO$_{N=3}$-ELBO$_{N=0}$=43.3 (Figure S3B). With the proposed ISME method, the optimal polynomial order was N=4. The corresponding increase in ELBO (ΔELBO=ELBO$_{N=4}$-ELBO$_{N=0}$=73.1) is higher than in data acquired with the standard multi-echo trajectory. Image-specific weights were computed as the inverse of the diagonal elements of the noise covariance matrix estimated by ReML. The dependence of the weights on the echo time of the data shows little change for values of N≥4 (Figure S3C).

2. Supplementary figures

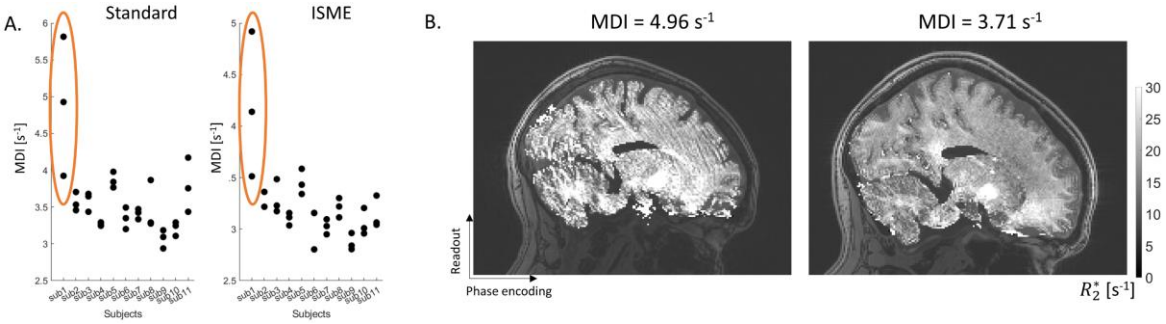

Figure S1: (A) Motion degradation index (MDI) of the datasets acquired with the standard multi-echo trajectory and ISME. The average MDI from subject 1 was 4.5±0.8s^{-1} and the average MDI amongst the other subjects was 3.3±0.3s^{-1}. (B) R_2* map computed from the first repetition of the standard multi-echo trajectory for subject 1 (MDI=4.96s^{-1}) and for one participant with MDI=3.71s^{-1}.

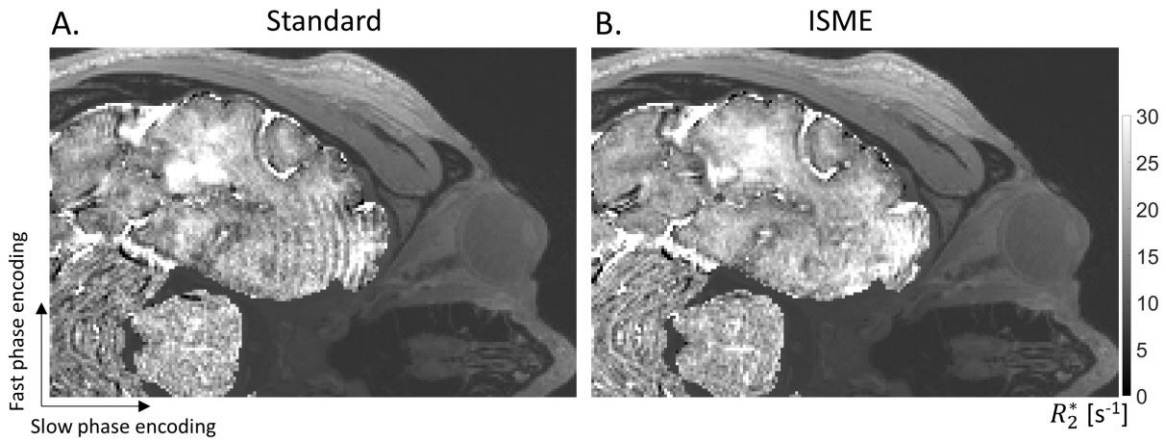

Figure S2: Eye movement during the acquisition of MRI data leads to image aliasing along the slow phase-encoding direction of a 3D-encoded image (blue arrows). This aliasing is present in data acquired with a standard multi-echo trajectory (A) but not with ISME (B).

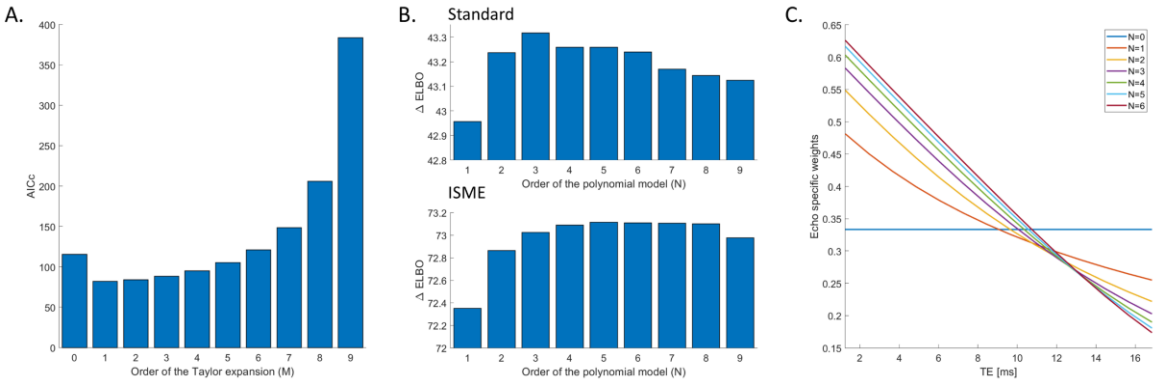

Figure S3: (A) Change in the Akaike information criterion (AICc) with the order of the Taylor expansion of the signal decay (M). (B) Increase of the evidence lower bound (ELBO) with the order of the polynomial model of the dependence of image noise on the echo time of the data (N), compared to N=0 (uniform noise level across echo times), for standard multi-echo trajectory and ISME. (C) Echo specific weights computed for different polynomial orders (M=2).